Lift capability improvement for an airfoil with filled cavity

Constantin Rotaru

***Abstract*—**This paper proposes an improved airfoil model for the helicopter rotor blade. This airfoil has a filled cavity on the upper surface where the filled body is a free rotating cylinder. The effect on the flow around the airfoil is the generation of vortices that reduce the flow separation downstream of the cavity. The CFD and vortex panel method results show an enhanced lift capability both for advancing and retreating helicopter rotor blade.

***Keywords*—**airfoil, helicopter aerodynamic, panel method, rotor blade, vortex strength.

I. Introduction

THE classical unsteady aerodynamic theories describing the observed behavior have formed the basis for many types of rotor analysis. The tools for the analysis of 2-D, incompressible, unsteady aerodynamic problems were extended to compressible flows, being a basis for developing linearized unsteady aerodynamic models applicable to compressible flows. At the blade element level, the various sources of unsteady effects can be decomposed into perturbations to the local angle of attack and velocity field. At low angle of attack with fully attached flow, the various sources of unsteady effects manifest as moderate amplitude and phase variations relative to the quasi-steady airloads. At higher angles of attack when time-dependent flow separation from the airfoil may be involved, a phenomenon characterized by large overshoots in the values of the lift, drag and pitching moment relative to the quasi-steady stall values, may occur.

One important parameter used in the description of unsteady aerodynamics und unsteady airfoil behavior is the reduced frequency, *k*, defined as $k = \omega \cdot c/(2V)$, where ω is the angular frequency, *c* is the chord of the airfoil and *V* is the flow velocity. According to the dimensional analysis, the resultant force, *F*, on the airfoil of chord *c*, can be written in functional form as $F/\left(\rho V^2 c^2\right) = f(Re, M, k)$. For $k = 0$ the flow is steady and for $0 \le k \le 0.05$ the flow can be considered quasi-steady, that is, unsteady effects are generally small.

Flows with characteristic reduced frequencies above of 0.05 are considered unsteady [1]. For a helicopter rotor in forward flight (fig. 1), the reduced frequency at any blade element can't be exactly calculated, but a first order approximation for *k*, can give useful information about the degree of unsteadiness.

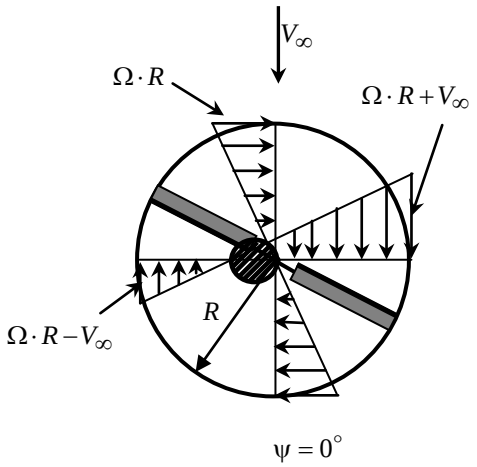

Fig. 1 helicopter main rotor

The problem of finding the airloads on an oscillating airfoil was solved by Theodorsen, who gave a solution to the unsteady airloads on a 2-D harmonically oscillated airfoil in inviscid, incompressible flow, with the assumption of small disturbances. Both the airfoil and its shed wake were represented by a vortex sheet with the shed wake extending as a planar surface from the trailing edge downstream to infinity. The assumption of planar wake is justified if the disturbances remain relatively small. As with the standard quasi-steady thin airfoil theory, the bound vorticity, γ_b, can sustain a pressure difference and, therefore, a lift force [2]. The wake vorticity, γ_w, must be force free with zero net pressure jump over the sheet. According to the Theodorsen's theory, the solution for the loading γ_b on the airfoil surface under harmonic forcing conditions is obtained from integral equation

$$w(x,t) = \frac{1}{2\pi}\int_0^c \frac{\gamma_b(x,t)}{x - x_0}dx + \frac{1}{2\pi}\int_c^\infty \frac{\gamma_w(x,t)}{x - x_0}dx \qquad (1)$$

where *w* is the downwash on the airfoil surface.

So long as the circulation about the airfoil is changing with respect to time, the circulation is continuously shed into the wake and will continuously affect the aerodynamic loads on the airfoil. For a general motion, where an airfoil of chord $c = 2b$ is undergoing a combination of pitching $(\alpha, \dot{\alpha})$ and plunging $(\dot{h})$ motion in a flow of steady velocity *V*,

Constantin Rotaru is with the Aviation Department, "Henri Coanda" Air Force Academy, Brasov, 500183, Romania, tel: +40745974488; e-mail: rotaru.constantin@afahc.ro.

Theodorsen's solution for the lift coefficient and pitching moment coefficient corresponding to mid-chord $M_{1/2}$ are

$$\begin{cases} c_l = \pi b\left[\frac{\ddot{h}}{V^2}+\frac{\dot{\alpha}}{V}-\frac{b}{V^2}a\ddot{\alpha}\right]+ \\ \quad +2\pi\left[\frac{\dot{h}}{V}+\alpha+\frac{b\dot{\alpha}}{V}\left(\frac{1}{2}-a\right)\right]C(k) \\ c_{m1/2}=\frac{\pi}{2}\left[\frac{ba\ddot{h}}{V^2}-\frac{b^2}{V^2}\left(\frac{1}{8}+a^2\right)\ddot{\alpha}\right]+ \\ +\pi\left(a+\frac{1}{2}\right)\left[\frac{\dot{h}}{V}+\alpha+b\left(\frac{1}{2}-a\right)\frac{\dot{\alpha}}{V}\right]C(k)-\frac{\pi}{2}\left[\left(\frac{1}{2}-a\right)\frac{b\dot{\alpha}}{V}\right] \end{cases} \quad (2)$$

where a is the pitch axis location relative to the mid-chord of the airfoil, measured in terms of semi-chord and $C(k)=F(k)+iG(k)$ is the complex transfer function (known as Theodorsen's function) which accounts the effects of the shed wake on the unsteady airloads,

$$C(k)=\frac{H_1^{(2)}(k)}{H_1^{(2)}(k)+i\cdot H_0^{(2)}(k)}= \\ \frac{J_1(J_1+J_0)+Y_1(Y_1-J_0)}{(J_1+Y_0)^2+(Y_0-J_1)^2}+i\frac{Y_1Y_0+J_1J_0}{(J_1+Y_0)^2+(Y_0-J_1)^2} \quad (3)$$

with J_0, J_1, Y_0, Y_1 being Bessel functions of the first and second kind, respectively (fig.2).

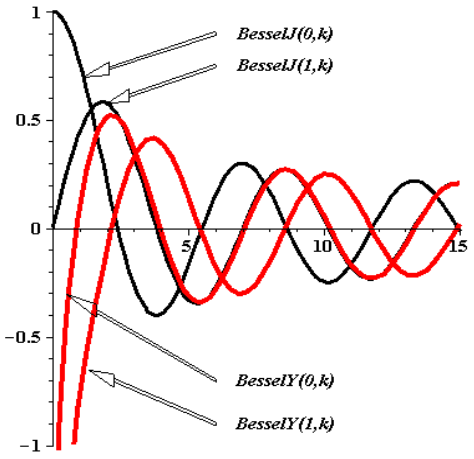

Fig. 2 Bessel functions

The real and imaginary parts of $C(k)$ function are plotted in fig. 3. It could be appreciated that $C(k)$ function serves to introduce an amplitude reduction and phase lag effect on the circulatory part of the lift response compared to the result obtained under quasi-steady conditions [3].

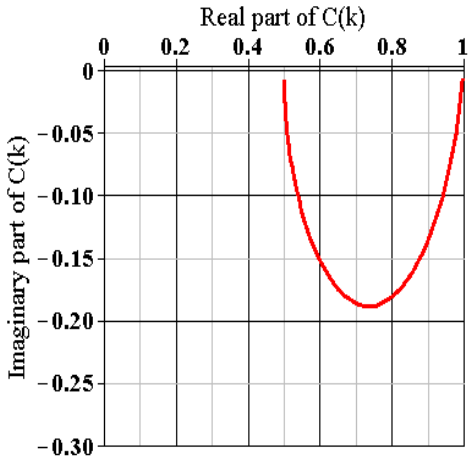

Fig. 3 Theodorsen's function

This effect can be seen if a pure oscillatory variation in angle of attack is considered, that is, $\alpha=\bar{\alpha}e^{i\omega t}$, so the circulatory part of the airfoil lift coefficient is given by

$$c_l=2\pi\bar{\alpha}C(k)=2\pi\bar{\alpha}\left[F(k)+iG(k)\right] \quad (4)$$

For $k=0$, the steady-state lift behavior is obtained, that is, c_l is linearly proportional to α. As k is increased, the lift plots develop into hysteresis loops and these loops rotate such that the amplitude of the lift response (half of the peak-to-peak value) decreases with increasing reduced frequency. These loops are circumvented in a counterclockwise direction such that the lift is lower than the steady value when α is decreasing with time (i.e., there is a phase lag). For infinite reduced frequency the circulatory part of the lift amplitude is half that at $k=0$ and there is no phase lag angle.

One of the most important characteristics used to judge the performance of an airfoil is the maximum static lift capability.

This is a quantity that is not easily predicted even with computational methods and experimental measurements. Even from an experimental perspective, absolute values of $C_{l\,max}$ are difficult to guarantee with high precision and especially between tests performed in different wind tunnels. The maximum lift that can be developed by an airfoil when operating at a steady angle of attack is related to the type of stall characteristic of that airfoil. At low speeds, airfoils generally fall into three static stall categories, namely thin airfoil stall, leading edge stall and trailing edge stall. The measurements show that thin airfoil and leading edge stalls can be fairly sensitive to changes in airfoil shape, whereas trailing edge stall is insensitive. Most conventional helicopter rotor airfoils fall into the category of trailing edge or leading edge stall types at low to moderate Mach numbers. It is also common for a mixed stall behavior to occur on some airfoils which is a stall characteristic that is not clearly one type or another [4].

Airfoils designed for helicopter applications have traditionally been obtained through a long evolutionary process in which various levels of theory and experimental

measurements have been combined in the pursuit of airfoil shapes with higher values of maximum lift, better lift-to-drag ratios, lower pitching moments and higher drag divergence Mach numbers. In general, these requirements are conflicting, making the design of general purpose rotor airfoils extremely challenging. Instead, various families of airfoils have been developed and optimized to meet the specific needs of different parts of the rotor blade. The use of different airfoils along the blade is made easier because of computer-aided design and composite manufacturing capability which involves only small additional costs over blade made with a single airfoil section [5].

The selection of airfoil sections for helicopter rotors is more difficult than for a fixed-wing aircraft because they are not point designs. For angle of attack and Mach number vary continuously at all blade elements on the rotor and one airfoil section cannot meet all the various aerodynamic requirements.

The rotor limits may be determined by either advancing blade compressibility effects or retreating blade stall. Because the onset of flow separation may limit rotor performance, there has been a great deal of emphasis in rotor design on maximizing the lifting capability of rotor airfoil sections to simultaneously alleviate both compressibility effects and retreating blade stall. The rotor design point must recognize the influence of both effects as limiting factors as well as allow sufficient margins from the stall/compressibility boundary for perturbations in angle of attack and Mach number associated with maneuvering flight and turbulent air.

The aerodynamic characteristics of rotor airfoils must be assessed at their actual operational Reynolds numbers and Mach numbers. The maximum lift coefficient, $C_{l\,max}$, can be used as one indicator of the significance of viscous effects. At the low end of the practical Reynolds number range for rotors, most airfoils have relatively low values of $C_{l\,max}$. This is because the viscous forces are more determinant, the boundary layer is thicker and the flow will separate from the airfoil surface [5].

At higher angles of attack the adverse pressure gradients produced on the upper surface of the airfoil result in a progressive increase in the thickness of the boundary layer and cause some deviation from the linear lift versus angle of attack behavior. On many airfoils, the onset of flow separation and stall occurs gradually with increasing of angle of attack but on some airfoil (those with sharp leading edges), the flow separation may occur quite suddenly. In the stalled flow regime, the flow over the upper surface of the airfoil is characterized by a region of fairly constant static pressure. The pitching moment about ¼-chord is much more negative because with the almost constant pressure over the upper surface the center of pressure is close to mid-chord. Less lift is generated by the airfoil because of the reduction in circulation and loss of suction near the leading edge and the drag is greater. Under these separated flow conditions, steady flow no longer prevails, with turbulence and vortices being ahead alternately from the leading and trailing edges of the airfoil into the wake [7].

The envelope of rotor thrust limits is the outcome of operation on the blades of stall effects at high angle of incidence and compressibility effects at high Mach number. Usually the restrictions occur within the limits of available power. In hover, conditions are uniform around the azimuth and blade stall sets a limit to the thrust available. As forward speed increases, maximum thrust on the retreating blade falls because of the drop in dynamic pressure and this limits the thrust achievable throughout the forward speed range. By the converse effect, maximum thrust possible on the advancing side increases but is unrealizable because of the retreating blade restriction. At higher speeds, as the advancing tip Mach number approaches 1.0, its lift becomes restricted by shock-induced flow separation, leading to drag or pitching moment divergence, which limits the maximum speed achievable. Thus, the envelope comprises a limit on thrust from retreating blade stall and a limit on forward speed from advancing blade Mach effects [8].

The ability to develop computers methods in performance calculation has been a major factor in the rapid development of helicopter technology. Results may often not be greatly different from those derived from the simple analytical formulae but the fact that the feasibility of calculation is not dependent upon making a large number of challengeable assumptions is important in pinning down a design, making comparisons with flight tests [9].

Helicopter rotor blades have a much stiffness and effective damping than the wing of a fixed wing aircraft for the in-plane degree of freedom. Whereas the blade flapping torsion degrees of freedom are influenced by the lift and pitching moment, the lead-lag degree of freedom is influenced by the drag. The blade lead-lag motion may couple with the flapping or torsion degrees and may lead to an aeroelastic instability of the blades. In the rotor plane there are a large number of vertical disturbances that lie in proximity to the blades, being significant on the advancing and retreating sides of the rotor, where the blades may interact with tip vortices.

II. HELICOPTER ROTOR BLADE AERODYNAMIC LIMITS

The rotor limits may be determined by two conditions, one codition given by advancing blade compressibility effects and the other one condition given by retreating blade stall. In either case the advancing blade operates at low angle of attack but at high subsonic or transonic conditions, whereas the retreating blade operates at low Mach numbers and high lift coefficients [10].

The region of the rotor disk affected by compressibility effects is shown in fig. 4 and is defined on the surface where the incident Mach number of the flow that is normal to the leading edge of the blade exceeds the drag divergence Mach number, M_{dd}. If $M_{\Omega R}$ is the hover tip Mach number, than the region of the disk affected by compressibility effects is defined by

$$M_{r,\psi} = M_{\Omega R}\left(r + \mu \sin\psi\right) \geq M_{dd} \tag{5}$$

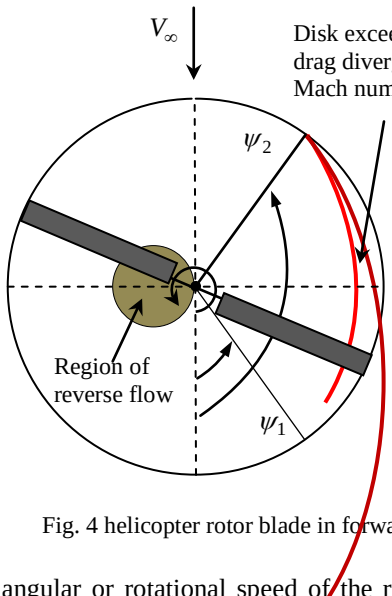

Fig. 4 helicopter rotor blade in forward flight

The angular or rotational speed of the rotor is denoted by Ω, the rotor radius by R, the advanced ratio $\mu = V_\infty \cos\alpha / \Omega R$ and $r = y/R$ where y is the axis along the rotor blade and α is the angle between the forward velocity V_∞ and the plane of the rotor [1, 2]. The azimuth angle for the onset drag divergence, ψ_1, can be obtained by setting $r = 1$, so that

$$\psi_1 = arcsin\left(\left[\frac{1}{\mu}\left(\frac{M_{dd}}{M_{\Omega R}} - 1\right)\right]\right) \quad (6)$$

and $\psi_2 = 180 - \psi_1$.

Another complication with helicopter rotors is that the wakes and tip vortices from other blades can lie close to each other and to the plane of blade rotation and so they have large induced effects on the blade lift distribution (fig. 5).

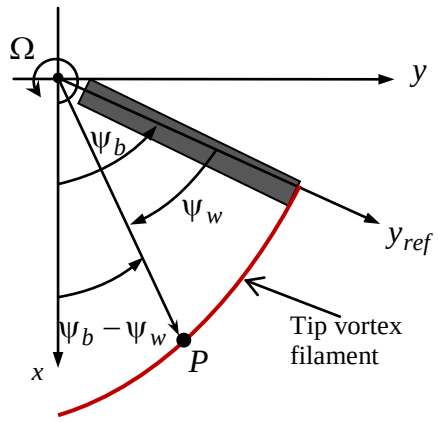

Fig. 5 tip vortex trajectory

If the wake is assumed to be undistorted in the tip path plane and no wake contraction occurs in the radial direction, then the tip vortex trajectories are described by the equations

$$\begin{cases} x = R\cos(\psi_b - \psi_w) + R\mu\psi_w \\ y = R\sin(\psi_b - \psi_w) \end{cases} \quad (7)$$

where ψ_b is the position of the blade when the vortex was formed and ψ_w is the position of the vortex element relative to the blade. These interactions of blades and tip vortices (called blade-vortex-interactions) can occur at many different locations over the rotor disk and also with different orientations.

III. Airfoil Blade with Filled Cavity

Two-dimensional simulations were performed for a standard NACA 2412 airfoil with and without cavity. Both edges of the cavity are sharp in order to fix the separation point (forward edge) and to maximize the feedback loop of the shear layer (rear edge). The cavity was filled with a rotating small cylinder for improving the circulation around the airfoil (fig. 6).

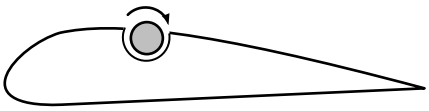

Fig. 6 airfoil with filled cavity

The computational domain extends to a distance of 12 chords lengths in the upstream and downstream directions and three chords lengths in the upper and lower normal directions. The distance between the discrete points at which the non-slip condition is enforced needs to be equal to or slightly greater than the grid spacing. The grid resolution and domain size were varied in order to assess convergence and influence of the far-field boundary condition. The Reynolds number was sufficiently high such that the formation of large scale vortices and the subsequent pairing of these structures gives rise to aperiodic low frequency oscillations that are difficult to characterize because the run times are not sufficiently long to observe many periods.

The CFD results are presented in the figures 7-10.

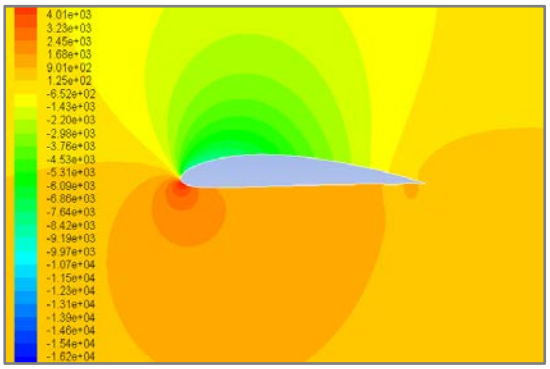

Fig. 7 airfoil without cavity: pressure distribution

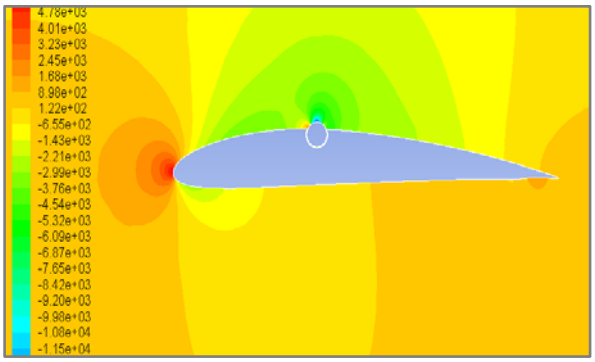

Fig. 8 airfoil with filled cavity: pressure distribution

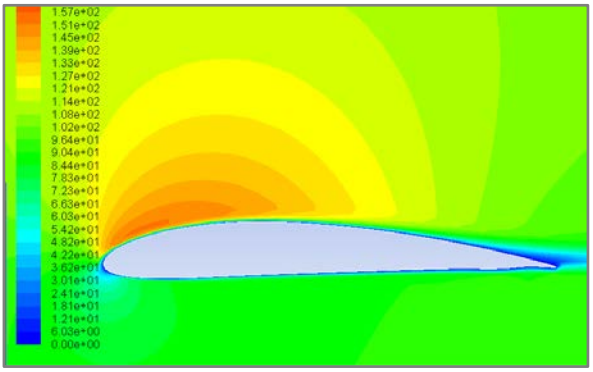

Fig. 9 airfoil without cavity: velocity distribution

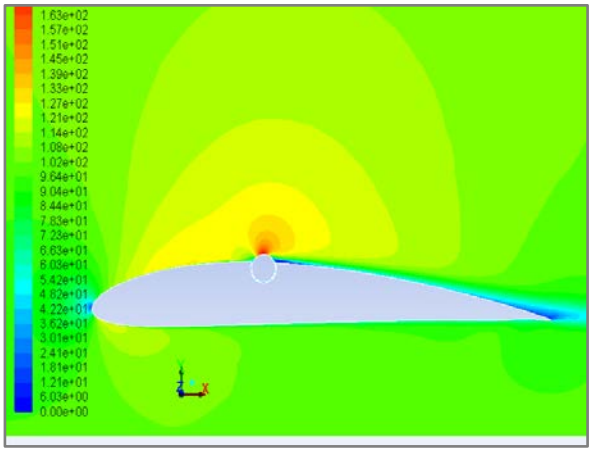

Fig. 10 airfoil with filled cavity: velocity distribution

The relative high thickness of the airfoil without a cavity causes a laminar separation which initially starts approximately half a chord length from the leading edge. At very high angles of attack the flow over the airfoil with cavity separates well before the forward edge of the cavity. The separated flow displays a strong interaction with the cavity and this interaction causes the flow to shed smaller scale structures than the airfoil without cavity at the same angle of attack.

IV. Panel Method Results

Potential flow over an airfoil of arbitrary shape can be synthesized by combining uniform flow with a curved vortex sheet wrapped around the surface of the airfoil. The concept of replacing the airfoil surface with a vortex sheet is more than just a mathematical device because there is a thin boundary layer on the surface, due to the action of friction between the surface and the airflow, in which the large velocity gradients produce substantial vorticity, hence, there is a distribution of vorticity along the airfoil surface due to viscous effects [5].

The vortex strength, $\gamma(s)$ must vary along the surface such that the normal component of velocity induced by the entire sheet and the uniform flow is zero everywhere along the surface of the airfoil. In most cases, the strength distribution necessary to satisfy this condition is difficult to be determined analytically. For numerical computations, such sheet can be approximated as a series of flat vortex panels wrapped around the surface of the airfoil (fig. 11).

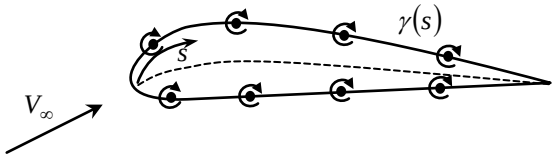

Fig. 11 vortex sheet

To define the vortex panels, a series of nodes is placed on the airfoil surface, such that the nodes are clustered more tightly near the leading and trailing edges. The change of variable $x/c = (1-\cos\theta)/2$ provides the desired clustering in x.

The panels start at the trailing edge, are spaced forward along the lower surface, are wrapped up around the leading edge and then run back along the upper surface to the trailing edge so that the last panel ends at the trailing edge where the first panel began. The vortex strength $\gamma(s)$ of each panel is assumed to be linear along the panel and continuous from one panel to the next. That is, for the n panels, the vortex panel strengths are $\gamma_1, \gamma_2, \ldots\ldots\gamma_n$, and the main thrust of the panel technique is to solve for γ_j, $j=1$ to n, such that the body surface becomes a streamline of the flow and such that the Kutta condition $\gamma_1 = -\gamma_n$ is satisfied (fig. 12).

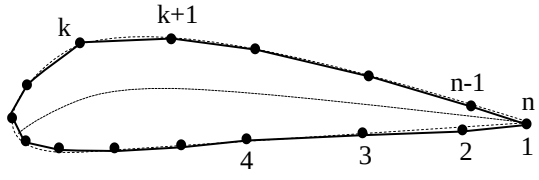

Fig. 12 vortex panel distribution

To solve for the n unknown nodal vortex strengths, at the center of each panel is defined a control point where the normal component of the flow velocity is imposed to be zero.

For an even number n of nodes, the points x_i, $i=1,2,.....n/2$ on the chord line are computed from the following algorithm:

$$\delta\theta=\frac{2\pi}{n-1},\ x_i=\frac{c}{2}\left\{1-cos\left[\left(i-\frac{1}{2}\right)\delta\theta\right]\right\},\ i=1,2,3,.....n/2$$

The lover and upper surface coordinates for an airfoil can be obtained from the camber line geometry, $y_c(x)$, and the thickness distribution, $t(x)$ as follows

$$\begin{cases} X_l(x_i)=x_i+\dfrac{t(x_i)}{2\sqrt{1+\left(\dfrac{dy_c(x)}{dx}\right)^2\Big|_{x=x_i}}}\dfrac{dy_c(x)}{dx}\Big|_{x=x_i} \\ Y_l(x_i)=y_c(x_i)-\dfrac{t(x_i)}{2\sqrt{1+\left(\dfrac{dy_c(x)}{dx}\right)^2\Big|_{x=x_i}}} \end{cases} \quad (8)$$

$$\begin{cases} X_u(x_i)=x_i-\dfrac{t(x_i)}{2\sqrt{1+\left(\dfrac{dy_c(x)}{dx}\right)^2\Big|_{x=x_i}}}\dfrac{dy_c(x)}{dx}\Big|_{x=x_i} \\ Y_u(x_i)=y_c(x_i)+\dfrac{t(x_i)}{2\sqrt{1+\left(\dfrac{dy_c(x)}{dx}\right)^2\Big|_{x=x_i}}} \end{cases} \quad (9)$$

For a point x_i on the chord line (fig. 13) we have two nodes on the airfoil, one node on the lower line of the airfoil, $P_{\frac{n}{2}+1-i}[X_l(x_1),Y_l(x_i)]$and the other one on the upper line of the airfoil, $P_{\frac{n}{2}+i}[X_u(x_1),Y_u(x_i)]$.

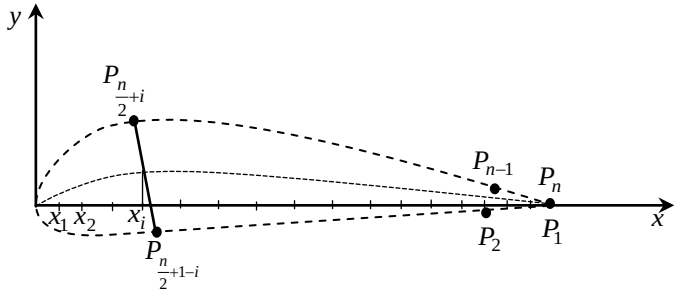

Fig. 13 the upper and lower lines nodes

A second-order panel method assumes a linear variation of $\gamma(s)$ over a given panel and the value of $\gamma(s)$ at the edges of each panel is matched to its neighbors (fig. 14). The flow-tangency boundary condition is still applied at the control point to each panel.

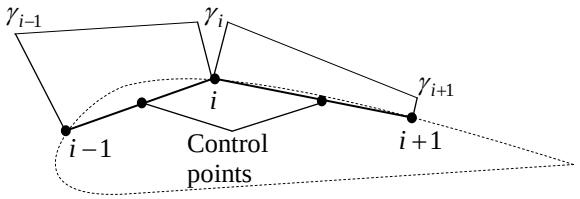

Fig. 14 linear distribution of $\gamma(s)$

The coordinates of these control points are given by

$$\begin{cases} X_C(i)=\dfrac{X_{P_i}+X_{P_{i+1}}}{2} \\ Y_C(i)=\dfrac{Y_{P_i}+Y_{P_{i+1}}}{2} \end{cases} \quad (10)$$

Each panel is assigned a local panel coordinate system (ξ,η) as shown in fig. 15.

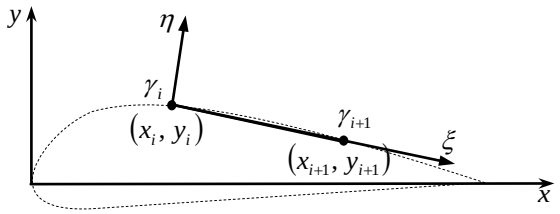

Fig. 15 vortex panel coordinate system

For each panel, an infinite number of infinitesimally weak vortices are combined in side-by-side fashion as shown in fig. 16.

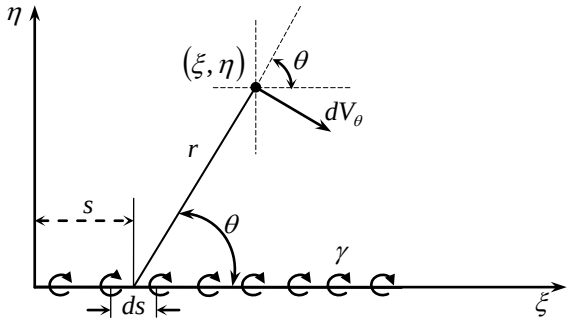

Fig. 16 edge view of a 2-D vortex panel

Consider a differential segment of a vortex panel that lies on the ξ axis at the location $\xi=s$ and has length ds. The velocity induced at any point (ξ,η) by this differential vortex is normal to the vector $\vec{r}$ and has a magnitude inversely proportional to the distance between the points of coordinates $(s,0)$ and (ξ,η), namely $r=|\vec{r}|$. The ξ- and η- components

of the velocity induced at the point (ξ,η) by this infinitesimally vortex panel are given by

$$\begin{cases} dV_\xi = dV_\theta \sin\theta = \dfrac{\gamma(s)}{2\pi r}\sin\theta\, ds \\ dV_\eta = -dV_\theta \cos\theta = -\dfrac{\gamma(s)}{2\pi r}\cos\theta\, ds \end{cases} \tag{11}$$

According to fig. 16 we have

$$\begin{cases} \sin\theta = \dfrac{\eta}{r} \\ \cos\theta = \dfrac{\xi - s}{r} \end{cases} \tag{12}$$

where $r = \sqrt{(\xi - s)^2 + \eta^2}$.

It follows that

$$\begin{cases} dV_\xi = \dfrac{\eta\,\gamma(s)}{2\pi\left[(\xi - s)^2 + \eta^2\right]}ds \\ dV_\xi = -\dfrac{((\xi - s))\gamma(s)}{2\pi\left[(\xi - s)^2 + \eta^2\right]}d \end{cases} \tag{13}$$

A linear vortex strength distribution on the panel *j* extending from $\xi = 0$ to $\xi = l_j$ has the expression

$$\gamma(s) = \frac{\gamma_{j+1} - \gamma_j}{l_j}s + \gamma_j \tag{14}$$

where

$$l_j = \sqrt{(x_{j+1} - x_j)^2 + (y_{j+1} - y_j)^2} \tag{15}$$

The matrix of the velocities V_ξ and V_η is

$$\begin{bmatrix} V_\xi \\ V_\eta \end{bmatrix} = \frac{1}{2\pi l_j}\begin{bmatrix} (l_j - \xi)B + \eta A & \xi B - \eta A \\ -l_j - (l_j - \xi)A + \eta B & l_j - \xi A - \varepsilon B \end{bmatrix}\cdot\begin{bmatrix} \gamma_j \\ \gamma_{j+1} \end{bmatrix} \tag{16}$$

where

$$\begin{cases} A = \dfrac{1}{2}ln\dfrac{\xi^2 + \eta^2}{(\xi - l_j)^2 + \eta^2} \\ B = arctan\dfrac{l_j - \xi}{\eta} + arctan\dfrac{\xi}{\mu} \end{cases} \tag{17}$$

In order to get the velocity induced by panel *j* at the control point of the panel *i*, the coordinates of control point must be expressed from the coordinate system (x, y) in the coordinate system (ξ,η) of panel *j*, making a rotation with angle β_j and a translation in the point (x_j, y_j) as it follows

$$\begin{cases} \sin\beta_j = \dfrac{y_{j+1} - y_j}{l_j} \\ \cos\beta_j = \dfrac{x_{j+1} - x_j}{l_j} \end{cases} \tag{18}$$

$$\begin{bmatrix} \xi_C(i) \\ \eta_C(i) \end{bmatrix} = \begin{bmatrix} \cos\beta_j & \sin\beta_j \\ -\sin\beta_j & \cos\beta_j \end{bmatrix}\cdot\begin{bmatrix} x_C(i) - x_j \\ y_C(i) - y_j \end{bmatrix} \tag{19}$$

$$\begin{bmatrix} V_x(i) \\ V_y(i) \end{bmatrix} = \begin{bmatrix} \cos\beta_j & -\sin\beta_j \\ \sin\beta_j & \cos\beta_j \end{bmatrix}\cdot\begin{bmatrix} V_\xi(i) \\ V_\eta(i) \end{bmatrix} =$$

$$= \frac{1}{2\pi l_j^2}\begin{bmatrix} x_{j+1} - x_j & -(y_{j+1} - y_j) \\ y_{j+1} - y_j & x_{j+1} - x_j \end{bmatrix}\cdot$$

$$\begin{bmatrix} (l_j - \xi_C(i))B + \eta_C(i)A & \xi B - \eta_C(i)A \\ -l_j - (l_j - \xi_C(i))A + \eta_C(i)B & l_j - \xi_C(i)A - \eta_C(i)B \end{bmatrix}\cdot\begin{bmatrix} \gamma_j \\ \gamma_{j+1} \end{bmatrix}$$

or

$$\begin{bmatrix} V_x(i) \\ V_y(i) \end{bmatrix} = \begin{bmatrix} P_{11}(j,i) & P_{12}(j,i) \\ P_{21}(j,i) & P_{22}(j,i) \end{bmatrix}\cdot\begin{bmatrix} \gamma_j \\ \gamma_{j+1} \end{bmatrix} \tag{20}$$

The velocities in the coordinate system (ξ_i, η_i) of the panel *i* are

$$\begin{bmatrix} V_\xi(i) \\ V_\eta(i) \end{bmatrix} = \begin{bmatrix} \cos\beta_i & \sin\beta_i \\ -\sin\beta_i & \cos\beta_i \end{bmatrix}\cdot\begin{bmatrix} V_x(i) \\ V_y(i) \end{bmatrix}$$

$$= \begin{bmatrix} \dfrac{x_{i+1} - x_i}{l_i} & \dfrac{y_{i+1} - y_i}{l_i} \\ -\dfrac{y_{i+1} - y_i}{l_i} & \dfrac{x_{i+1} - x_i}{l_i} \end{bmatrix}\cdot\begin{bmatrix} P_{11}(j,i) & P_{12}(j,i) \\ P_{21}(j,i) & P_{22}(j,i) \end{bmatrix}\cdot\begin{bmatrix} \gamma_i \\ \gamma_{i+1} \end{bmatrix} \tag{21}$$

The velocity $V_\eta(i)$ induced in the control point of panel *i* by panel *j* is

$$V_\eta(i) = \left(-\frac{y_{i+1} - y_i}{l_i}P_{11}(j,i) + \frac{x_{i+1} - x_i}{l_i}P_{21}(j,i)\right)\gamma_i + \left(-\frac{y_{i+1} - y_i}{l_i}P_{12}(j,i) + \frac{x_{i+1} - x_i}{l_i}P_{22}(j,i)\right)\gamma_{i+1} \tag{22}$$

The $n \times n$ airfoil coefficient matrix M is generated from the 2×2 panel coefficient matrix in airfoil coordinates, $P(i, j)$ for the velocity induced at the control point *i* by panel *j*, extending from node *j* to node $j+1$, and the *n* nodal vortex strengths, γ_1 through γ_n are then obtained by numerically solving the linear system

$$M\cdot\begin{bmatrix} \gamma_1 \\ \gamma_2 \\ \dots \\ \gamma_{n-1} \\ \gamma_n \end{bmatrix} = V_\infty\begin{bmatrix} [(y_2 - y_1)\cos\alpha - (x_2 - x_1)\sin\alpha]/\, l_1 \\ [(y_3 - y_2)\cos\alpha - (x_3 - x_2)\sin\alpha]/\, l_2 \\ \dots\dots\dots\dots\dots\dots\dots\dots\dots\dots\dots\dots \\ [(y_n - y_{n-1})\cos\alpha - (x_n - x_{n-1})\sin\alpha]/\, l_{n-1} \\ 0.0 \end{bmatrix}$$

Once the nodal strengths are known, the velocity and pressure at any point in space can be computed by adding the velocity induced by all $n-1$ vortex panels in the free stream velocity,

$$\begin{bmatrix} V_x \\ V_y \end{bmatrix} = V_\infty \begin{bmatrix} cos\,\alpha \\ sin\,\alpha \end{bmatrix} + \sum_{i=1}^{n-1} \begin{bmatrix} V_x(i) \\ V_y(i) \end{bmatrix} \quad (23)$$

The lift coefficient for the entire airfoil is the sum of those induced by all the $n-1$ panels,

$$C_l = \sum_{i=1}^{n-1} \frac{l_i}{c} \cdot \frac{\gamma_i + \gamma_{i+1}}{V_\infty} \quad (24)$$

V. Results

For the clean airfoil at $\alpha = 0^\circ$ the flow initially separates around 50% of the chord length and this separation causes a periodic vortex shedding in the wake of the airfoil. At $\alpha = 10^\circ$ and $\alpha = 15^\circ$ the separation bubble and the vortex structures are larger and the separation point on the suction side moves upstream with increasing the angle of attack. The separated vortices tend to merge into larger structures before being shed into the wake.

The filled cavity has a strong influence on the structure of the flow in the separation bubble. It promotes smaller-scale vortex shedding than would otherwise occur for the airfoil without a cavity at the same angle of attack.

VI. Conclusions

The section lift coefficients predicted by thin airfoil theory and panel codes are in good agreement with experimental data for low Mach numbers and small angles of attack. The airfoil with filled cavity gives good results regarding the maximum lift coefficient and the behavior of the helicopter retreating blade.

References

[1] J. G. Leishman, *Principles of Helicopter Aerodynamics*, Cambridge University Press, 2007.

[2] J. Seddon, S. Newman, "*Basic Helicopter Aerodynamics*", AIAA Education Series, Reston Virginia, USA, 2001.

[3] C. Rotaru, "Nonlinear Characteristics of Helicopter Rotor Blade Airfoils: An Analytical Evaluation," *Mathematical Problems in Engineering*, vol. 2013, Article ID 503858, 9 pages, 2013.

[4] R. Prouty, Helicopter Performance, Stability and Control, Krieger Publishing Company, Florida, USA, 2002.

[5] J. Katz, A. Plotkin, "Low Speed Aerodynamics" Cambridge University Press, 2010.

[6] C. Rotaru, I. Circiu, M. Boscoianu, "Computational Methods for the Aerodynamic Design", Review of the Air Force Academy, No 2(17)/2010, p. 43-48.

[7] D. Sakhr and V. Horak "Effect of Free-stream Turbulence Properties on Boundary Layer Laminar-Turbulent Transition: A new Approach, *9th International Conference Mathematical Problems in Engineering, Aerospace and Sciences (ICNPAA 2012)*, Book Series AIP Conference Proceedings, Volume 1493, Pages 282-289, Published 2012.

[8] C. Rotaru, A. Arghiropol, "Maple soft solutions for nonlifting flow over arbitrary bodies", *Proceedings of the 3rd WSEAS International Conference on FINITE DIFFERENCES-FINITE ELEMENTS-FINITE VOLUMES-BOUNDARY ELEMENTS*, ISSN 1790-2769, pp 270-274, Romania, 2010.

[9] M. Boşcoianu, R. Pahonie, C. Rotaru, I. Fuiorea, N. Popoviciu „A Method to Predict the Flapping Wing MAV Global Aerodynamic Performances", Proceedings of the 6th IASME International Conference on Fluid Mechanics and Aerodynamics", ISBN 978-960-6766-98-5, Pages 190-195, Published 2008.

[10] C. Rotaru, M. Andres-Mihăilă, P. G. Matei, R. I. Edu, "*Dynamics of a Turbojet Engine Considered a Quasi-static System*", International Journal of Mechanics, ISSN 1998-4448, Volume 8, Pages 158-166, 2014.